small methods
www.small-methods.com

Improved Crystallization of Lead Halide Perovskite in Two-Step Growth Method by Polymer-Assisted "Slow-Release Effect"

*Siyuan Lin, Shuyue Wu, De'en Guo, Han Huang, Xuefan Zhou, Dou Zhang, Kechao Zhou, Wenhao Zhang, Yue Hu, Yongli Gao, and Conghua Zhou**

Fast reaction between organic salt and lead iodide always leads to small perovskite crystallites and concentrated defects. Here, polyacrylic acid is blended with organic salt, so as to regulate the crystallization in a two-step growth method. It is observed that addition of polyacrylic acid retards aggregation and crystallization behavior of the organic salt, and slows down the reaction rate between organic salt and PbI_2, by which "slow-release effect" is defined. Such effect improves crystallization of perovskite. X-ray diffraction study shows that, after addition of 2 mM polyacrylic acid, average crystallite size of perovskite increases from ≈40 to ≈90 nm, meanwhile, grain size increases. Thermal admittance spectroscopy study shows that trap density is reduced by nearly one order (especially for deep energy levels). Due to the improved crystallization and reduced trap density, charge recombination is obviously reduced, while lifetime of charge carriers in perovskite film and devices are prolonged, according to time-resolved photoluminescence and transient photo-voltage decay curve tests, respectively. Accordingly, power conversion efficiency of the device is promoted from 19.96 (±0.41)% to 21.84 (±0.25)% (with a champion efficiency of 22.31%), and further elevated to 24.19% after surface modification by octylammonium iodide.

1. Introduction

Organic–inorganic hybrid perovskite (PVSK) has become an important material in the application of photovoltaic technique owning to its high extinction coefficient,[1] low binding energy of exciton,[2] as well as suitable optical band gap,[3] and thus prompt the fast development of perovskite solar cells (PSCs). Photo-to-electric power conversion efficiency (PCE) of the PSCs has increased from 3.81% in 2009 to the recently recorded 25.7%,[4–7] though still below the theoretical limit of 33%.[8] As such, much works are needed. It is well known that, high quality PVSK film is of critical essence for realizing high-performance PSCs.[9–11] "High-quality" means pin-hole free and less defective. Right now, PVSK films are mainly prepared by solution basing methods, like one-step,[12] or two-step solution[13] process, blade coating,[14] slot die,[15] and so on. Besides, thermal evaporation has also been applied.[16] Due to the fast volatilization of solvent and also the relative low nucleation/crystallization barrier,[17] PVSK growth by solution methods is usually finished within a relative short period, for example, few to tens of minutes. Such process quickly leads to the risk of obtaining low quality films, for example, pinholes,[18] small crystallites/grains,[19] or poly boundaries,[13,20] which brings risk of short-circuiting, concentrated defects, and thus deteriorates device efficiency and stability.[21]

In order to improve the crystallization, many efforts have been proposed. In 2014, Huang et al. treated the PVSK film by "solvent annealing" technique, and obtained pin-hole free, well-crystallized film with grain size up to 1 μm, which helped to achieve PCE of 15.6% in methylammonium (MA) basing

S. Lin, S. Wu, D. Guo, H. Huang, C. Zhou
Hunan Key Laboratory of Super-microstructure and Ultrafast Process
Hunan Key Laboratory of Nanophotonics and Devices
Institute of Super-microstructure and Ultrafast Process in Advanced Materials (ISUPAM)
School of Physics and Electronics
Central South University
Changsha, Hunan 410083, P. R. China
E-mail: chzhou@csu.edu.cn

The ORCID identification number(s) for the author(s) of this article can be found under https://doi.org/10.1002/smtd.202201663

DOI: 10.1002/smtd.202201663

X. Zhou, D. Zhang, K. Zhou
State Key Laboratory of Powder Metallurgy
Powder Metallurgy Research Institute
Central South University
Changsha, Hunan 410083, P. R. China

W. Zhang, Y. Hu
Michael Grätzel Center for Mesoscopic Solar Cells
Wuhan National Laboratory for Optoelectronics
Huazhong University of Science and Technology
Wuhan, Hubei 430074, P. R. China

Y. Gao
Department of Physics and Astronomy
University of Rochester
Rochester, New York, NY 14627, USA

PSCs.[22] Han et al. observed that the interaction between DMSO and PbI_2 could benefit the crystallization of PVSK.[23] In 2019, Kim et al. observed that methylammonium chloride (MACl) could regulate the formation dynamics of formamidinium-based perovskite ($FAPbI_3$), and obtained PCE of 24.02%.[24] More impressively, to slow down the crystallization processes of PVSK in the so-called triple mesoscopic skeleton, Han et al. introduced *N*-methylformamide (NMF) into the PVSK precursor, which controlled the crystallizing process in a closed chamber, and helped to obtain PCE of 18.82% in the carbon-electrode based, hole-conductor-free mesoscopic PSCs.[25] Similar work was done by You et al. in the crystallization of $CsPbI_3$.[26] In 2021, Ding et al. applied a cooling stage to slowing down the appearing velocity of $FAPbI_3$ nucleation, and also upgraded PVSK crystallization and device efficiency.[27] As such, controlling the crystallization process is efficient in high-efficiency device fabrication.

In addition, to reduce the defects in PVSK, polymer molecules have also been imported. For example, in 2017, Yang et al. blended poly (4-vinylpyridine) (PVP) in PbI_2 precursor solution so as to passivate uncoordinated Pb^{2+}, by which both efficiency and stability were improved.[28] In 2019, Liao et al. introduced polyinylidene fluoride-trifluoroethylene polymer (PVDF-TrFE) into PVSK, which enhanced the build-in field and upgraded PCE.[19] Besides, polyacrylonitrile (PAN),[29] polyethylene glycol(PEG),[30] polymerized methyl methacrylate (PMMA) have also been applied.[31] These polymers not only regulated the crystallization process, but also passivate the defects.

It is noticed that, during the two-step growth method, most of the strategies are focused on the PbI_2 side, while less has been done to the organic salt. Honestly, organic salt is quite easy to aggregate and crystallize, which could affect PVSK growth. To manipulate the crystallization process, attention should also be paid to the organic salt side. As a result, here in this article, a kind of long chain polymer or polyacrylic acid (PAA) is used to mix with organic salt. As will be shown later, PAA could strongly interact with the organic cations, and slow down the reaction rate between organic salt and PbI_2, by which a kind of "slow-release effect" is observed. In fact, such effect is widely used in medicine science. It means that the "functional factors" could be released slowly, which helps to reach more effective functionality. As will be shown later, such effect could obviously improve the crystallization quality, cut down defects, and hence reduce recombination risk, and upgrade device efficiency and stability.

2. Results and Discussion

2.1. "Slow-Release Effect" Brought by PAA and the Effect on the Crystallization of PVSK in Two-Step Growth Method

It is observed that, adding PAA could slow down the reaction between PbI_2 and organic cations. The effect is clearly depicted in **Figure 1**a and Video S1, Supporting Information. After addition of PAA, color of PVSK films changes more slowly. For example, after being kept for 960 s (16 min), the pristine film turns dark red, while it remains red for that blended with PAA. As such, PAA has slowed down the reaction between organic salt and PbI_2. Such phenomenon is ascribed to the "slow-release effect." To verify such effect, interaction between organic salt and PAA molecules are examined through Fourier transform infrared (FTIR) study. As is shown in Figure 1b, after PAA blending, the stretch mode of –N-H group (from FA+ cation FAI) shifts from 3356.96 to 3362.55 cm^{-1}, indicating that chemical interaction might happen with –N-H group. To clarify the interaction, PAA is also monitored by FTIR before and after mixing with FAI. As is shown in Figure 1b, vibration of "–C=O" group shifts from 1712.59 to 1716.65 cm^{-1} after FAI mixing, showing that the chemical interaction appears for –C=O. Considering the molecule structure of FAI and PAA, the interaction should be existing between groups of "–C=O" and "FA+," in addition, "hydrogen bond" might appear due to the static electrical force.[32–34] Such interaction could hinder the diffusion of organic cations into the PbI_2 matrix, and lower down the reaction between them. As a result, it is more difficult for the coated film to turn black. Moreover, XRD study shows that the crystallization of FAI film could be obviously inhibited by PAA (Figure 1c,d). For example, there is a strong diffraction peak at around 25.8° in pristine FAI film, with intensity of 18 003; after PAA blending, the intensity of the peak drops down to 1839, being reduced by almost ten times, indicating that PAA has inhibited the crystallization behavior of the organic salt. Again, the retarded crystallization of FAI is due to the interaction between PAA and organic cations. To show clearly about the functionality of "slow-release effect," schematic diagrams are shown in Figure 1e,f.

The interaction could further be reflected from the morphology observations. As shown in Figure 1c,d, without PAA blending, inhomogeneous film is obtained, with aggregates and pinholes. After PAA blending, the film becomes more uniform and compact. The improved film quality could also be reflected from the optical photograph (Figure S1, Supporting Information). On the other hand, the improved film continuity could be contributed by the long chain feature of PAA. Accordingly, we can see that, PAA has brought a kind of "slow-release effect" to the organic salt, and two merits could be quickly obtained: i) PAA can slow down the diffusion rate of FAI in to PbI_2 matrix, which cuts down the crystallization rate of PVSK. ii) It increases the coverage of FAI on PbI_2, which makes it easier to grow uniform PVSK film. These merits help to regulate the crystallization process of PVSK.

To show the role of "slow-release effect" in the coarsening dynamics of the PVSK films, and hence the power conversion properties of the devices, the concentration of PAA is adjusted in organic salt matrix. **Figure 2**a–d shows the top-view scanning electron microscope (SEM) images of PVSK films. Without PAA, inhomogeneous and porous surface of pristine PVSK films is observed; after incorporation of PAA, uniform and compact film is seen, along with larger gains. Cross-section SEM images (the insets) show similar result. Uniform and compact PVSK grains could be seen after PAA blending. However, after the doping concentration increases up to 4 mM, there exists a number of small particles on the surface (red circle in Figure 2d), showing that too concentrated doping would deteriorate crystallization due to the steric effect of polymer molecules. Statistics are performed on grain size according to the SEM images. As is shown in Figure 2e–h, the average grain size is 868.3, 903.2, 984.9, and 1006.4 nm, corresponding to the concentration of PAA with 0, 1, 2, and 4 mM, respectively. The increased grain size results from the favored crystallization process by slow-release effect. Larger grains are helpful in reducing grain boundaries, as such, less

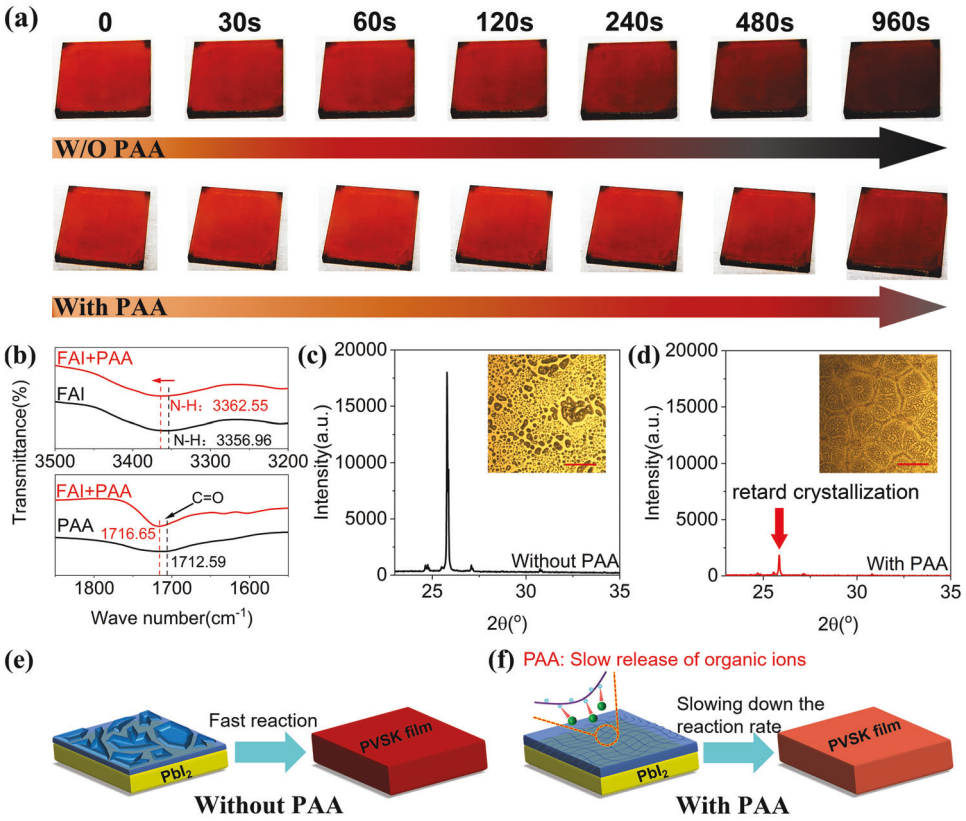

Figure 1. a) Color evolution of the PVSK films recorded after coating of organic salt solution on PbI_2. b) Fourier transform infrared (FTIR) spectra of –N-H group in FAI and –C=O group in PAA. X-ray diffraction (XRD) spectra of FAI films: c) before and d) after PAA blending (inset shows the metallographic photos of FAI films prepared by spin-coating under room temperature, no thermal annealing is used; the scale bar is 100 μm). Schematic diagram of "slow-release effect": e) without PAA and f) with PAA.

defects are anticipated, as will be shown later. Atomic force microscope (AFM) study shows that PAA blending could flatten the surface. As is shown in Figure 2i–l, the root mean square roughness (RMS) decreases from 27.9 to 21 nm as the concentration rises from 0 to 4 mM. The increased grain size shows improvement on the crystallization, which will be reflected from the XRD study. Then the reduced RMS is due to upgraded continuity of FAI. Both of them are brought by the "slow-release effect."

Crystallization quality is studied by XRD; the results are shown in **Figure 3**a. Meanwhile, the full width at half magnitude (FWHM) of the peak (110) is collected, which is shown in Figure 3b. It is 0.19° for the pristine PVSK film, while decreasing to 0.08° after moderate concentration blending (2 mM case). The average crystallite size is estimated according to the Sherrer's formula:

$$D = \frac{k\lambda}{\beta \cos\theta} \tag{1}$$

where k is the Scherrer constant and equaling to 0.89, λ is 0.154 nm, β is the FWHM, θ is the diffraction angle, D is the average crystallite size (nm). Also shown in Figure 3b, the average crystallite size increases from 42.34 nm (pristine film) to 95.40 nm (2 mM case), clearly showing that the crystallization has been upgraded. As such, the polymer assisted "slow-release effect" is beneficial for PVSK crystallization in the two-step growing method. Again, slowing down the coarsening rate could promote the growth of PVSK crystals. In fact, similar behavior could be seen single-crystalline silicon, or single PVSK crystalline growth.[35,36] The improved crystallization helps to upgrade the extinction behavior of PVSK. As is shown in Figure 3c, after PAA blending, higher absorbance is seen at long wavelength region (550–750 nm). Steady photoluminescence (PL) test observes that, after PAA blending, PL peak shifts from 810 to 805 nm. As is shown in Figure S2, Supporting Information, when incident laser is guided from the substrate side, blue shift is also observed in 4 mM case. Time-resolved photoluminescence (TRPL) is tested; the results are shown in Figure 3d. Life time of charge carriers in PVSK film (τ_{film}) is calculated according the procedure described in Supporting Information (along with Table S1, Supporting Information).[37] It is 2.10, 2.29, 3.17, and 2.03 μs for blending concentration of 0, 1, 2, and 4 mM, respectively, which is also shown in inset of Figure 3d. Noting that, the prolonged lifetime is close to that observed in literatures.[5,38] The blue shift (in steady PL test) and the prolonged lifetime (in TRPL test) are ascribed to the reduced defects. To verify this assumption, thermal admittance spectroscopy (TAS) is adopted. Angular frequency dependent capacitance is measured under dark condition, and then

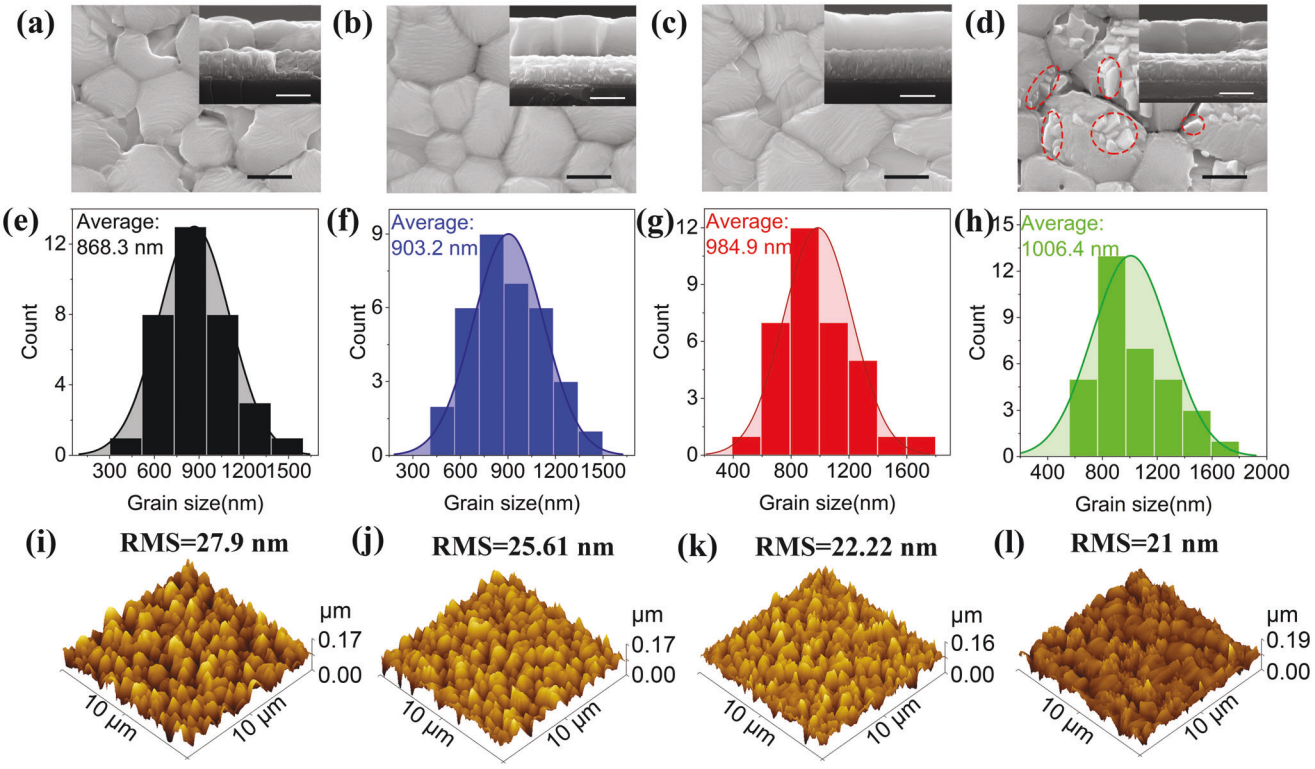

Figure 2. Top view scanning electron microscope (SEM) images of PVSK films grown with PAA blending (mM): a) 0, b) 1, c) 2, and d) 4. The red circle is defined as the small particles. The insets show relating cross-sectional SEM images. All scale bars are 500 nm. Statistics are performed on grain size for the PVSK films with organic salt blended by PAA (mM): e) 0, f) 1, g) 2, and h) 4. Atomic force microscope (AFM) images of PVSK films with PAA blending (mM): i) 0, j) 1, k) 2, and l) 4.

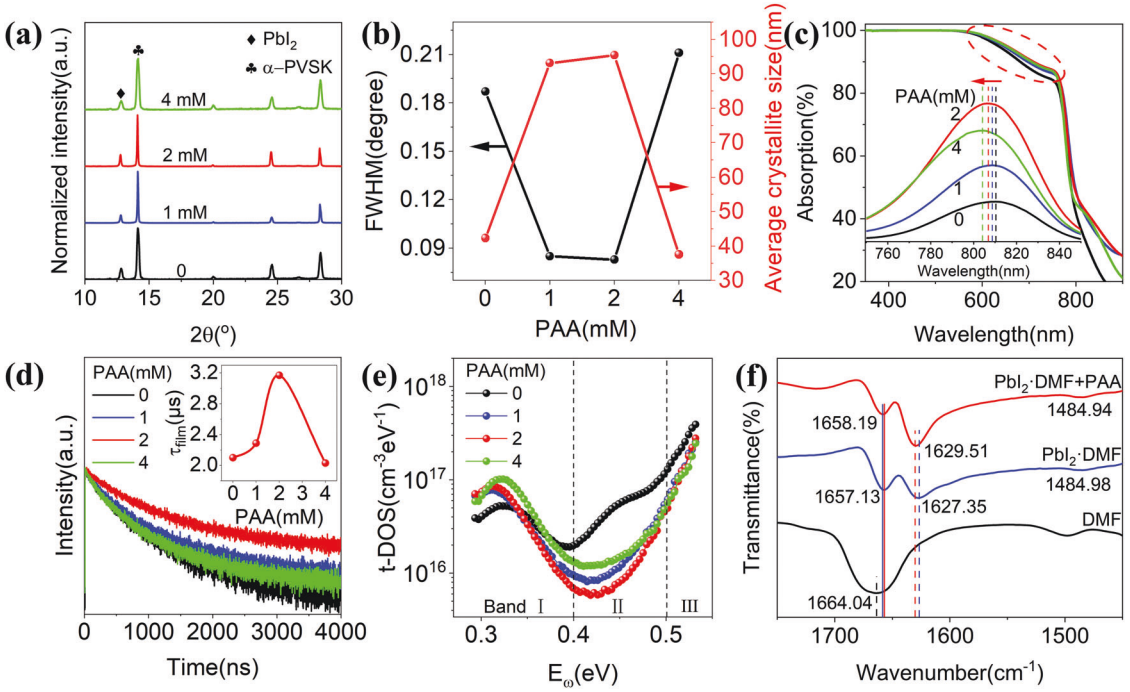

Figure 3. a) XRD pattern of PVSK films. b) Full width at half magnitude (FWHM) and average crystallite size. c) Absorption spectra of PVSK films (inset shows steady photoluminance spectra). d) Time-resolved photoluminance (TRPL) spectra of PVSK films deposited on glass slides. Inset shows related lifetime of PVSK film. e) Trap density of states (t-DOS) of PVSK. f) FTIR spectra of DMF, and PbI_2·DMF powder before and after PAA blending.

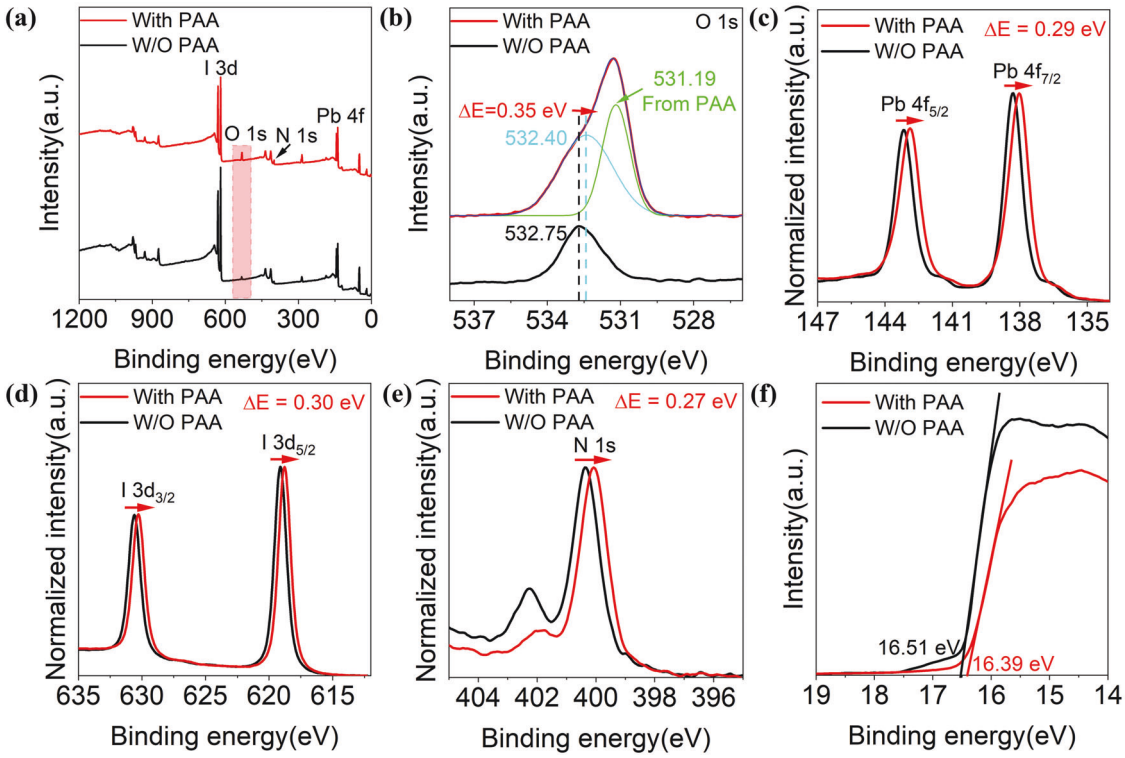

Figure 4. X-ray photoelectron spectrum (XPS) of: a) Full spectrum, b) O 1s, c) Pb 4f, d) I 3d, and e) N 1s. f) Secondary electron cutoff of UV photoelectron spectrum (UPS) (He I, $h\nu = 21.22$ eV) of PVSK films.

the density of state for traps (t-DOS) is derived using following formula:[39,40]

$$NT(E\omega) = -\frac{V_{bi}}{eW}\frac{\omega}{K_B T}\frac{dC}{d\omega} \quad (2)$$

$$E\omega = K_B T \ln\left(\frac{\omega_0}{\omega}\right) \quad (3)$$

where C is the capacitance, ω the angular frequency, ω_0 the attempt-to-escape frequency, e the elementary charge, K_B the Boltzmann's constant, and T the absolute temperature, V_{bi} the built-in potential extracted from the Mott–Schottky analysis, W the thickness of the active layer. As is shown in Figure 3e, for pristine PVSK film, t-DOS is among 1×10^{16} to 1×10^{17} cm^{-3} eV^{-1}. After PAA blending, it is reduced. Especially for the case of 2 mM case, about one order reduction is harvested in the deep level region (or bond II according to literature).[41] The reduced t-DOS is ascribed to two aspects: one is the upgraded crystallization which reduces grain boundaries and surface areas and then the defects density. The other is the passivation brought by PAA molecule to the un-coordinated Pb (II). Figure 3f shows FTIR spectra for DMF, PbI_2·DMF powders before and after PAA blending. It is seen that, after PbI_2 addition, –C=O group in DMF shifts from 1664.04 to 1627.35 cm^{-1}, which is due the interaction between PbI_2 and DMF.[42,43] However, after PAA blending, the peak moves back to 1629.51 cm^{-1}, this peak shift is ascribed to the formation of a coordinate bond between "–C=O" group (from PAA) and un-coordinated Pb (II).[28,44,45] Previous studies showed that, the un-coordinated Pb (II) caused traps in deep energy levels.[46,47] As such, the interaction is helpful to reduce deep level traps.

X-ray/UV photoelectron spectrum (XPS/UPS) studies are used to examine the effect of PAA on electronic structure of PVSK. The full spectrum of XPS is shown in **Figure 4**a and peak of O 1s is presented in Figure 4b. There are two O 1s peaks for PVSK doped with PAA, a lower one at 531.19 eV, and a higher one at 532.40 eV. However, only one O 1s peak is seen for pristine PVSK (lying at 532.75 eV). Generally, the lower one is corresponding to the absorbed O_2 from air, and the higher one come from the –C=O of PAA,[48] indicating that PAA molecules are left in PVSK films. As is shown in Figure 4c, after PAA blending, binding energy of Pb 4f5/2 shifts from 143.16 to 142.87 eV, while that of Pb 4f7/2 shifts from 138.30 to 138.03 eV. Negative shift of 0.29 eV (Pb 4f5/2) and 0.27 eV (Pb 4f7/2) is obtained. Similar phenomenon is observed for I 3d and N 1s. Negative shift of 0.30 eV and 0.27 eV is observed, as shows in Figure 4d,e, respectively. Again, O 1s from absorbed oxygen (Figure 4b) also shows negative shift of 0.35 eV. These shifts are possibly due to the lowering down of Fermi-level as will be discussed later.

UPS measurement shows that the work function (WF) changes after PAA blending. From the secondary electron cutoff shown in Figure 4f, one can see that, WF changes from 4.71 to 4.83 eV according to of the formula of WF = 21.22 eV − E_{cutoff}. As such, the Fermi level (E_f) also lowers down after PAA blending, which means that electrons at core level becomes easier to be excited by incident photons, which possibly cause negative shift for these four kinds of elements (O, Pb, I, N) from PVSK matrix. The rising work function might relate to two factors. One is the band

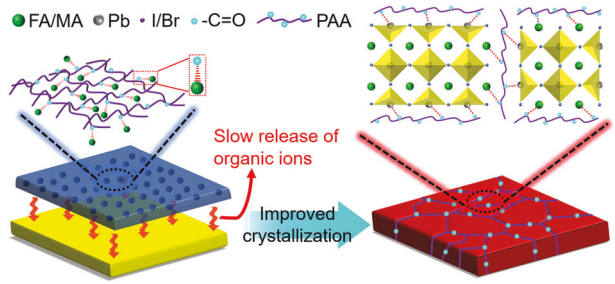

Figure 5. Schematic diagram to show the "slow-release effect" brought by PAA molecules and the role in upgrading PVSK crystallization.

bending behavior, which is brought by the surface dipoles.[49] Due to PAA blending in the organic salt, PAA molecules are easy to be left on surface, thus forming dipoles. The other possible factor is the "self-doping behavior." For example, Huang et al. previously observed that, residential I^- could make the PVSK film p-type, which could also lower down the Fermi level.[50] However, more studies are needed to clarify such feature.

To better understand the "slow-release effect," a schematic is shown in **Figure 5**. Due to the chemical interaction between PAA molecule and organic ions, a homogeneous and continuous organic salt layer can be formed. Due to the "slow-release effect" diffusion rate of organic ion is slowed down, which also reduces the reaction rate between organic ions and PbI_2. Due to the slowed reaction rate, PVSK nuclei could grow more slowly, which helps to achieve higher crystallization quality.

2.2. Power Conversion Properties of Perovskite Solar Cells with Respect to "Slow-Release Effect"

Charge transfer and recombination kinetics is studied with combination of transient photovoltage/photocurrent (TPC/TPV) and impedance spectra (IS). Typical TPC/TPV and Nyquist plots are shown in **Figure 6**a–c. Charge extraction time (t_d) is collected from the TPC curves, and the results are shown in inset of Figure 6a. It starts from 3.88 (±0.22) µs for pristine devices, then decreases to 3.68 (±0.33), 2.77 (±0.44) µs and rises to 4.69 (±0.25) µs after PAA blending at 1, 2, and 4 mM, respectively. Lifetime of charge carriers in devices (τ_{cell}) is fitted from the TPV curves, and the results are picked in Figure 6b. It is 14.01 (±1.29) µs for pristine case, then increases to 18.50 (±1.12), 22.84 (±2.80), and 34.29 (±6.82) µs after PAA blending of 1, 2, and 4 mM, respectively. As has been observed before, similar trend is observed between V_{oc} and τ_{cell}, showing prolonged lifetime of photo-generated charge carriers in device could make elevated V_{oc}.[51–54] Consequently, the charge transition process is accelerated and the lifetime of photo-generated charge carriers is extended. Typical IS curves are shown in Figure 6c, charge transfer/recombination resistance (R_{ct}/R_{re}) is fitted. The results are shown in Figure 6d. For R_{ct}, it is 7.05 (±2.07) × 10^4 ohm for pristine case, then decreases to 5.12 (±0.78), 3.07 (±0.92) × 10^4 ohm and rises to 5.77 (±0.67) × 10^4 ohm, after PAA blending of 1, 2, and 4 mM; As for R_{re}, it is 0.64 (±0.17) × 10^7 ohm for pristine case, then increases to 1.44 (±0.63), 3.69 (±1.73) × 10^7 ohm and decreases to 0.93 (±0.14) × 10^7 ohm for blending concentration of 1, 2, and 4 mM, respectively. Therefore, PAA blending improves charge extraction and reduces charge recombination. Again, above observation is due to two aspects: i) The improved crystallization that driven by the PAA assisted "slow-release effect," ii) passivation behavior of PAA molecule on Pb (II).

Dependence of open circuit voltage (V_{oc}) on light intensity (I_p), or V_{oc}–I_p curves are recorded, and the ideal factor (n) is calculated according to the following formula:[55]

$$Voc \propto \frac{nK_B T}{e} \ln I_P \tag{4}$$

where n, K_B, T, and I_p are ideal factor, Boltzmann's constant, absolute temperature, and light intensity, respectively. As is seen in Figure 6e, n is 1.70 for the pristine device, while decrease to 1.33 for PAA blending, indicating reduction in defects in the device. Moreover, Mott–Schottky study is performed, and capacitance–voltage (C^{-2}–V) curves are obtained, by which the built-in potential (V_{bi}) is fitted:

$$C^{-2} = \frac{2(V_{bi} - V)}{A^2 Nq\epsilon\epsilon_0} \tag{5}$$

where c, V, A, N, q, ϵ, and ϵ_0 are capacitance, bias, active area, concentration of donor-dopant, elementary charge, relative permittivity, and permittivity of free space, respectively. As show in Figure 6f, V_{bi} increases gradually from 0.78 to 1.03 V, which is consistent with that of V_{oc}. Such phenomenon is due to the passivation on defect.

PSCs with planar structure of "FTO/SnO_2/PVSK/Spiro-OMeTAD/Ag" are fabricated. As is shown in Figure S3, Supporting Information, thickness of the PVSK layer is about 600 nm. Photo-to-electric power conversion properties are examined with respect to PAA blending. Typical current density–voltage (J–V) curves are depicted in **Figure 7**a. Corresponding performance parameters are collected in Table S2, Supporting Information. As for pristine case, V_{oc} of 1.08 V, short-circuit current density (J_{sc}) of 24.84 mA cm^{-2}, fill factor (FF) of 76.14%, as well as PCE of 20.52% are obtained. Then for moderate PAA blending case (2 mM), V_{oc} of 1.11 V, J_{sc} of 25.37 mA cm^{-2}, FF of 79.04%, and PCE of 22.31% are harvested. External quantum efficiency (EQE) is tested, the results are shown in Figure 7b, the integrated J_{sc} is 24.61 and 23.67 mA cm^{-2} for PAA blending (2 mM), and pristine case, respectively, which matches 97% and 95% to the JV-recorded current densities for each.

For detailed comparison, effects of PAA concentration on the four performance parameters are depicted in Figure 7c–f. With concentration increasing, V_{oc} gradually increases from 1.08 (±0.01) to 1.11 (±0.01) V, J_{sc} raises from 24.61 (±0.51) to 25.16 (±0.21) mA cm^{-2}, FF increases from 75.22 (±1.46)% to 78.29 (±1.37)%. Accordingly, PCE upgrades from 19.96 (±0.41)% to 21.84 (±0.25)% (22.31% for the optimized). Careful examination shows that, J_{sc} moves in a contrast direction to t_d, showing that accelerated charge extraction is beneficial to the output of J_{sc}. The improved J_{sc} is partially due to enhanced absorption of light owing to increased crystallinity, the improved FF is due to the retarded charge recombination, and also the accelerated charge transfer. Hysteresis index (HI) of devices is calculated, and statistics are performed. As is shown in Figure S4, Supporting Information, PAA could slightly reduce the HI, though 2 mM doping

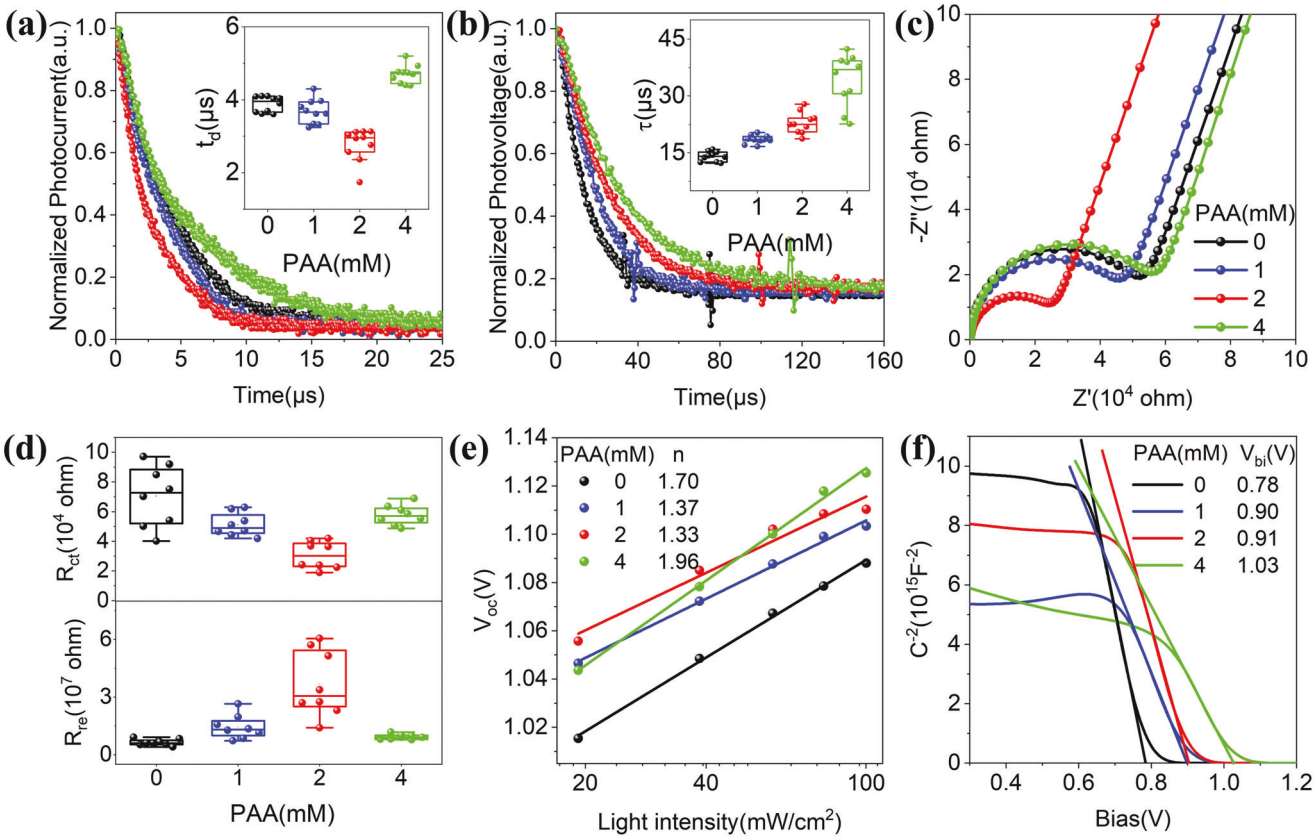

Figure 6. a,b) Transient photovoltage/photocurrent (TPC/TPV) decay curves. c) Nyquist plots curves. d) Statistics of R_{re} and R_{ct} picked from IS studies. e) Plotting between V_{oc} and light intensity. f) C^{-2}–V curves recorded from Mott–Schottky study.

produces the smallest. Hysteresis is usually observed in PSCs, it relates closely to ion migration in PVSK.[56]

Humidity resistance of PVSK film is studied by "water immersion test" experiment. As is shown in **Figure 8**a and Video S2, Supporting Information, after PAA doping, the PVSK degrades more slowly. Without doping, it turns yellowish completely in 2 s; after PAA doping, it becomes slightly yellowish after immersion for 60 s. As such, PAA can improve the humidity resistance of PVSK film. Such behavior is due to two factors: one is the interaction between PAA and organic ions, and the other is the improved crystallization of PVSK films. Similar behavior was observed in previous study.[57] Photo-stability and storage-stability are evaluated. As shown in Figure 8b, better photo-stability is harvested after moderate PAA blending. As for the storage-stability, after being stored in open air (devices unpackaged, relative humidity or RH is ≈35%) for 65 days, PAA blending devices could maintain about 83% of the original PCE, compared to that of 60% for pristine devices (Figure 8c).

2.3. Further Upgrading on Device Efficiency

In fact, device efficiency could be further upgraded after modifying PVSK by octylammonium iodide (OAI).[58,59] Crystallographic structure of the PVSK is examined by XRD. As is shown by Figure S5, Supporting Information, a new peak appears at about 3.6°, which is due to the so-called 2D phase of PVSK.[60] Then power conversion properties are evaluated. As is shown in **Figure 9**a, PAA blending helps to obtain V_{oc} of 1.16 V, J_{sc} of 25.20 mA cm^{-2}, FF of 82.46% and PCE of 24.19%, compared to 1.16 V, 24.94 mA cm^{-2}, 79.64% and 23.02% for devices without PAA blending. EQE spectrum is recorded. As is shown in Figure 9b, spectral response is slightly increased for PAA case.

The integrated current densities are 24.55 and 24.12 mA cm^{-2} for PAA-blending and control devices, respectively. Photostability is tested by performing quasi-maximum power point tracking (Q-MPPT). As is shown in Figure 9c, PAA-device shows stabilized power output about 24.06%, comparing to 22.29% of the control device. The upgraded device efficiency is due to OAI modification, which could turn the surface layer into 2D PVSK and passivate the surface defects.[61,62]

3. Conclusion

In summary, PAA is blended with organic salt during the two-step growth of perovskite. Due to the interaction between the function group of carbonyl (–C=O) and organic cations, a kind of "slow-release effect" is observed, which slows down the reaction rate between the organic cation and PbI_2 matrix, and upgrades the crystallization quality of the perovskite. Passivation behavior also appears due to the interaction between the carboxyl group and Pb (II). According to these two merits, t-DOS is reduced, and

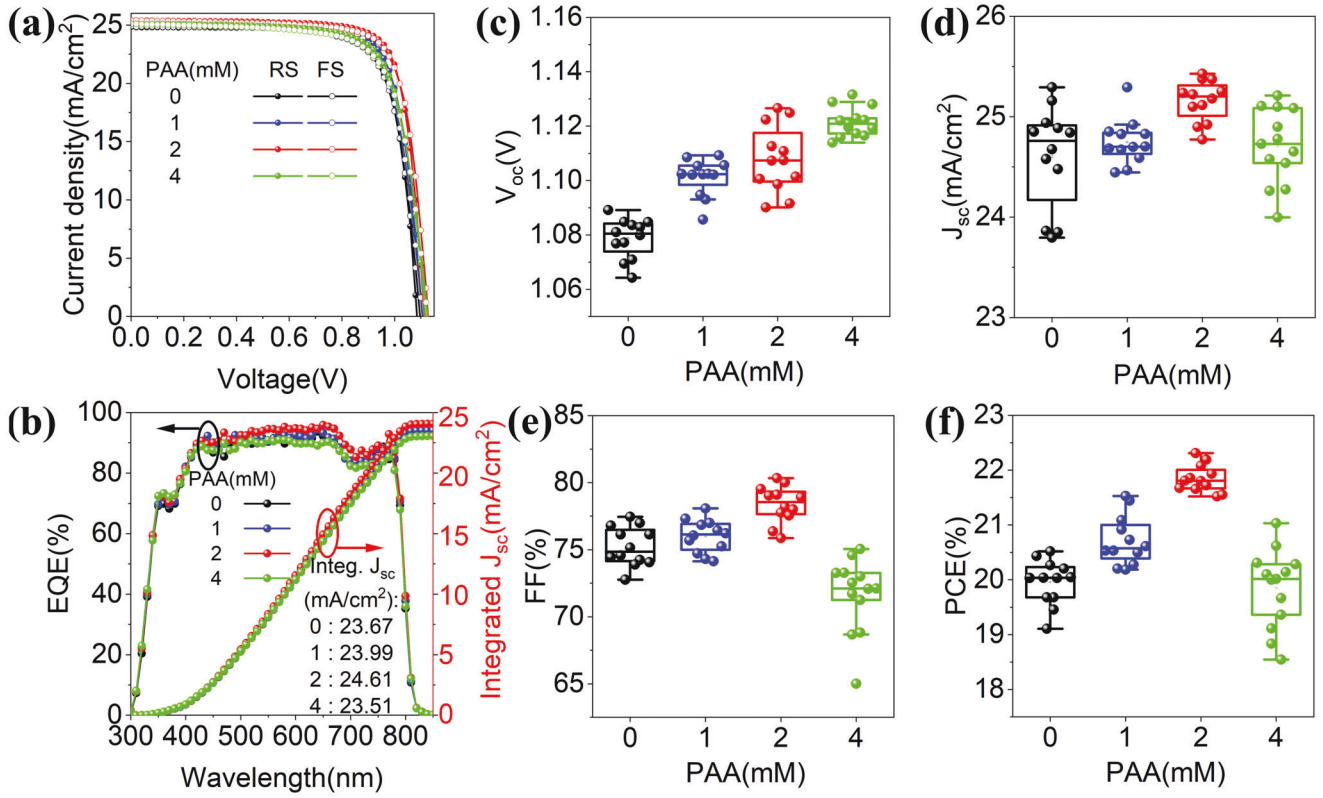

Figure 7. a) Typical current density–voltage (*J–V*) curves (recorded under simulated illumination of AM 1.5G, with the intensity of 100 mW cm^{-2}). b) The external quantum efficiency (EQE) spectra and integrated photocurrent. Statistics on performance parameters: c) V_{oc}, d) J_{sc}, e) FF, and f) *PCE*.

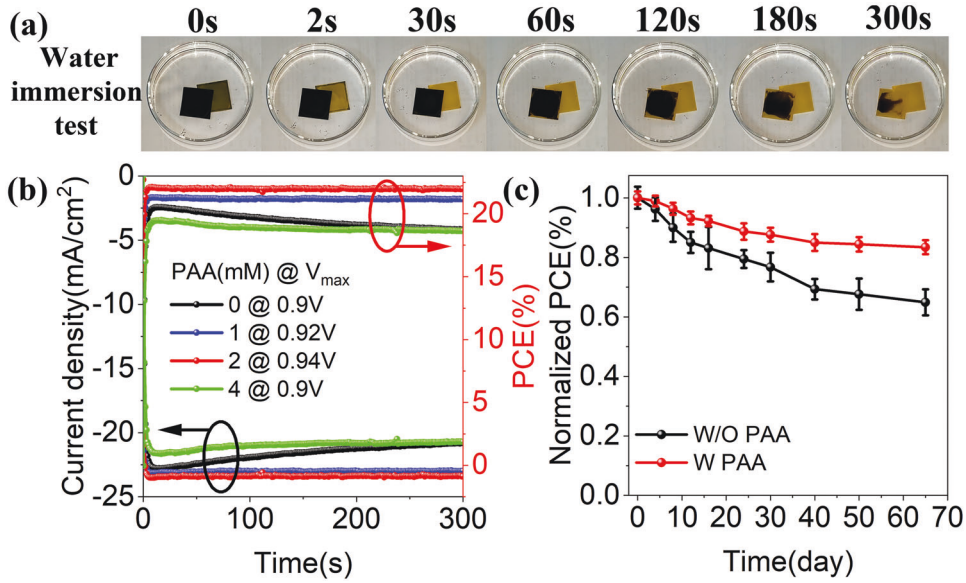

Figure 8. a) Water immersion test for PVSK films with organic salt doped by PAA (left, the doping concentration is 8 mg mL^{-1}) or not (right). b) Quasi-maximum power point tracking Q-MPPT test. c) Stability test, whereas the devices were kept in air (≈35% RH) and dark environment, and no encapsulation was used.

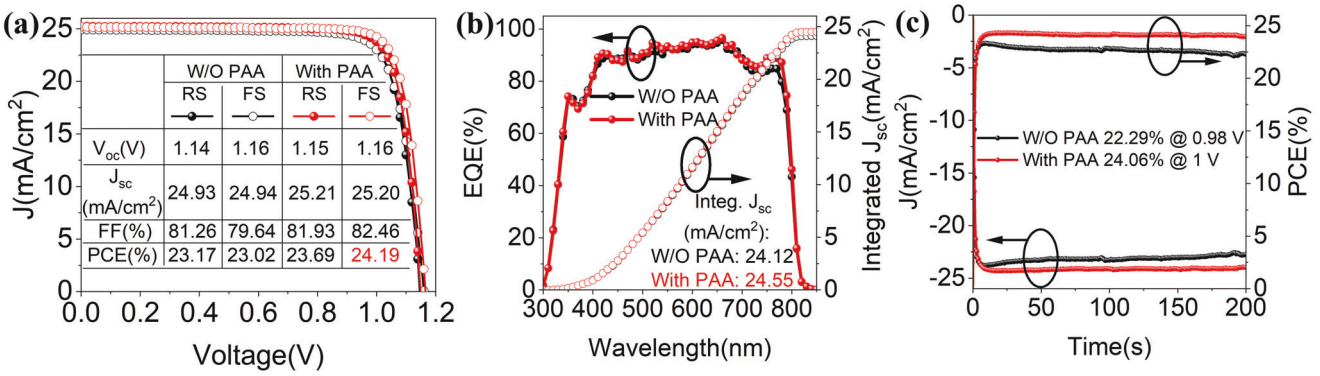

Figure 9. Effect of OAI based surface modification on power conversion properties of PSCs: a) Current density–voltage curve. b) External quantum efficiency (EQE) spectra and integrated photocurrent of champion device. c) Quasi-maximum power point tracking (Q-MPPT) test.

recombination is efficiently prevented, by which the efficiency and stability of device is improved.

4. Experimental Section

Materials: Tin (II) chloride dihydrate ($SnCl_2{\cdot}2H_2O$) was purchased from Sinopharm. Polyacrylic acid (PAA, M_W = 2000) was purchased from Aladdin. FTO, Lead iodide (PbI_2) and 2,2′,7,7′-tetrakis (*N*, *N*-di-p-methoxyphenylamine)–9, 9 spirobifluorene (Spiro-OMeTAD) were purchased from Advanced Election Technology Co., Ltd., formamidinium iodide (FAI), methylammonium chloride (MACl), methylammonium bromide (MABr), octylammonium iodide (OAI) were all purchased from Xi'an Polymer Light Technology Corp. Dimethylformamide (DMF), dimethyl sulfoxide (DMSO), chlorobenzene (CB), tert-butylpyridine (t-BP), and bis (trifluoromethanesulfonyl) imide (Li-TFSI) were purchased from Sigma-Aldrich. All the chemicals and reagents were used as received, without any further purification. Deionized water was prepared in laboratory.

Materials Synthesis: SnO_2 quantum dots (SnO_2 QDs) precursor was prepared using the method described as following: Typically and at first, 1.354 g $SnCl_2{\cdot}2H_2O$ was dissolved in 50 mL ethanol, being stirred vigorously until complete dissolution, then 10 mL of DI water was slowly added and followed by stirring for 48 h to form SnO_2 QDs. PbI_2 precursor was prepared by dissolved 553 mg PbI_2 in mixture solvent between DMF and DMSO (volume ratio of DMF : DMSO = 9.5:0.5, 1 mL), being stirred for overnight at 70 °C. Organic salt solution was prepared by dissolving 60 mg FAI, 6 mg MABr, and 8.2 mg MACl in 1 mL IPA. For PAA blending, certain volume of PAA solution (4 mM) was added, after which the concentration of PAA was 0, 1, 2, and 4 mM, respectively. For hole-transporting layer, 145 mg Spiro-OMeTAD powder was dissolved in 1750 µL CB with addition of 35 µL Li-TFSI solution (dissolved in acetonitrile, 1.81 M), 58 µL 4-tBP and 500 µL PMMA solution (dissolved in CB, with concentration of 0.24 M). All solutions were filtered by a 0.22 µm filter before use.

Device Fabrication: First, FTO substrates were ultrasonically cleaned in deionized water, acetone, and isopropyl alcohol each for 20 min. After drying in oven, FTO substrates were treated by UV/Ozone for 20 min. Then, SnO_2 QDs precursor was spin-coated on top with speed of 3000 rpm for 30 s, followed by 150 °C annealing in atmospheric environment for 1 h to form compact SnO_2 ETL. After that, SnO_2 films were treated by UV/Ozone for 20 min before PVSK fabrication. PVSK was fabricated by two-step process: PbI_2 solution was spin-coated on FTO/SnO_2 substrate by 2000 rpm for 30 s, and then annealed at 70 °C for 5 min, after cooling to room temperature, organic salt solution was spin-coated on top by speed of 2000 rpm for 20 s. Then, the wet films were annealed at 145 °C for 20 min in ambient air (30–40% RH). For OAI modification, OAI/IPA solution (4 mg mL^{-1}) was spin-coated on PVSK surface by speed of 4000 rpm for 30 s, and then annealed at 100 °C for 5 min. The hole-transport layer was deposited on top of PVSK by spin-coating the spiro-OMeTAD solution at 3000 rpm for 20 s. Finally, 100 nm Ag was thermal evaporated on top.

Material Characterization and Device Performance Evaluation: Morphological properties of PVSK were characterized by atomic force microscope (AFM 5500, Agilent). The surface and cross-sectional images of PVSK were characterized by scanning electron microscopy (SEM, TESCAN MIRA3 LMU). Crystallization of PVSK film was characterized X-ray diffraction (XRD) (D8 Advance, Bruker). Fourier transform infrared (FTIR) was conducted with Nicolet 6700 under air environment. The steady-state photoluminescence (PL) was recorded using a HITACHI F4700 spectrofluorometer with 600 nm of excitation wavelength. Extinction spectra of perovskite films were recorded by UV–vis spectrophotometer (UV7500, PuXi, Shanghai). Time-resolved photoluminescence (TRPL) was measured at 810 nm by HORIBA Scientific DeltaFlex fluorimeter with 478 nm excitation laser. Element analysis was performed by X-ray photoelectron spectrum (XPS, Thermo Fisher Scientific, monochromatized Al source with $h\nu$ = 1486.6 eV). Energy band analysis was characterized by UV photo-electron spectrum (UPS, Thermo Fisher Scientific, monochromatized He I source with $h\nu$ = 21.22 eV). External quantum efficiency (EQE) was tested by spectrum performance testing system (7-SCSpec, Beijing) with AC mode. Transient photovoltage/photocurrent (TPV/TPC) decay curves were measured by a home-made system equiped with a digital oscilloscope (DSO-X 3104A, Keysight) and N_2 laser (NL100, 337 nm, Stanford). For TPV measurement, background open circuit voltage (V_{oc}) of about 1050 mV was generated by static illumination; laser pulse was imported to generate ΔV_{oc} of about 5% of the background one. Impedance spectrum (IS) was carried out by electrochemical workstation (CHI 660D, Chenhua) with frequency range: 0.1 Hz to 1 MHz under open circuit and dark condition. The obtained spectra were fitted by homemade software. Current density–voltage curves were recorded by a digital sourcemeter (model 2400, Keithley Inc.) under simulated illumination (Enlitech SS-F7-3A, AM1.5 G), with intensity being calibrated to be 100 mW cm^{-2} by standard silicon cell (SRC-1000-TC-QZ-N, Enlitech). Devices were measured by reverse scan (1.2–0 V, with step of 0.02 V) and forward scan (0–1.2 V, with step of 0.02 V) with a mask area of 0.0514 cm^2. Capacitance–frequency (*c–f*) was measured by E4990A Precision LCR Meter (Keysight) in the range from 20 Hz to 2 MHz.

Supporting Information

Supporting Information is available from the Wiley Online Library or from the author.

Acknowledgements

C.Z. thanks the financial support of the National Natural Science Foundation of China (NSFC, No. 61774170), the Natural Science Foundation of

Hunan Province (No. 2020JJ4759), and the Key Scientific Research Project of Education Department of Hunan Province (22A0005). Y.G. acknowledges the support from the National Science Foundation, United States (NSF No. DMR-1903962). Y.H. acknowledges the support from the National Natural Science Foundation of China (NSFC, No. 22075094).

Conflict of Interest

The authors declare no conflict of interest.

Data Availability Statement

The data that support the findings of this study are available in the main text and the supplementary material of this article.

Keywords

defects, organic salts, polyacrylic acid, crystallization, slow-release effect

Received: December 15, 2022
Revised: February 5, 2023
Published online: February 28, 2023

[1] S. De Wolf, J. Holovsky, S. J. Moon, P. Loper, B. Niesen, M. Ledinsky, F. J. Haug, J. H. Yum, C. Ballif, *J. Phys. Chem. Lett.* **2014**, *5*, 1035.
[2] A. Miyata, A. Mitioglu, P. Plochocka, O. Portugall, J. T.-W. Wang, S. D. Stranks, H. J. Snaith, R. J. Nicholas, *Nat. Phys.* **2015**, *11*, 582.
[3] S. P. Pang, H. Hu, J. L. Zhang, S. L. Lv, Y. M. Yu, F. Wei, T. S. Qin, H. X. Xu, Z. H. Liu, G. L. Cui, *Chem. Mater.* **2014**, *26*, 1485.
[4] M. Kim, J. Jeong, H. Lu, T. K. Lee, F. T. Eickemeyer, Y. Liu, I. W. Choi, S. J. Choi, Y. Jo, H.-B. Kim, S.-I. Mo, Y.-K. Kim, H. Lee, N. G. An, S. Cho, W. R. Tress, S. M. Zakeeruddin, A. Hagfeldt, J. Y. Kim, M. Grätzel, D. S. Kim, *Science* **2022**, *375*, 302.
[5] Y. Zhao, F. Ma, Z. Qu, S. Yu, T. Shen, H.-X. Deng, X. Chu, X. Peng, Y. Yuan, X. Zhang, J. You, *Science* **2022**, *377*, 531.
[6] A. Kojima, K. Teshima, Y. Shirai, T. Miyasaka, *J. Am. Chem. Soc.* **2009**, *131*, 6050.
[7] Best Research-Cell Efficiency Chart.
[8] W. Shockley, H. J. Queisser, *J. Appl. Phys.* **1961**, *32*, 510.
[9] M. Saliba, J. P. Correa-Baena, M. Gratzel, A. Hagfeldt, A. Abate, *Angew. Chem., Int. Ed.* **2018**, *57*, 2554.
[10] G. E. Eperon, V. M. Burlakov, P. Docampo, A. Goriely, H. J. Snaith, *Adv. Funct. Mater.* **2014**, *24*, 151.
[11] S. Tombe, G. Adam, H. Heilbrunner, D. H. Apaydin, C. Ulbricht, N. S. Sariciftci, C. J. Arendse, E. Iwuoha, M. C. Scharber, *J. Mater. Chem. C* **2017**, *5*, 1714.
[12] M. M. Lee, J. Teuscher, T. Miyasaka, T. N. Murakami, H. J. Snaith, *Science* **2012**, *338*, 643.
[13] Z. Xiao, C. Bi, Y. Shao, Q. Dong, Q. Wang, Y. Yuan, C. Wang, Y. Gao, J. Huang, *Energy Environ. Sci.* **2014**, *7*, 2619.
[14] Y. Xiao, C. Zuo, J. X. Zhong, W. Q. Wu, L. Shen, L. Ding, *Adv. Energy Mater.* **2021**, *11*, 2100378.
[15] A. Verma, D. Martineau, E. Hack, M. Makha, E. Turner, F. Nüesch, J. Heier, *J. Mater. Chem. C* **2020**, *8*, 6124.
[16] M. Liu, M. B. Johnston, H. J. Snaith, *Nature* **2013**, *501*, 395.
[17] D. T. Moore, H. Sai, K. W. Tan, D. M. Smilgies, W. Zhang, H. J. Snaith, U. Wiesner, L. A. Estroff, *J. Am. Chem. Soc.* **2015**, *137*, 2350.
[18] A. Dubey, N. Adhikari, S. Mabrouk, F. Wu, K. Chen, S. Yang, Q. Qiao, *J. Mater. Chem. A* **2018**, *6*, 2406.
[19] C. C. Zhang, Z. K. Wang, S. Yuan, R. Wang, M. Li, M. F. Jimoh, L. S. Liao, Y. Yang, *Adv. Mater.* **2019**, *31*, 1902222.
[20] Y. P. Han, H. B. Xie, E. L. Lim, D. Q. Bi, *Sol. RRL* **2022**, *6*, 2101007.
[21] C. Ma, N.-G. Park, *Chem* **2020**, *6*, 1254.
[22] Z. Xiao, Q. Dong, C. Bi, Y. Shao, Y. Yuan, J. Huang, *Adv. Mater.* **2014**, *26*, 6503.
[23] Y. Wu, A. Islam, X. Yang, C. Qin, J. Liu, K. Zhang, W. Peng, L. Han, *Energy Environ. Sci.* **2014**, *7*, 2934.
[24] M. Kim, G.-H. Kim, T. K. Lee, I. W. Choi, H. W. Choi, Y. Jo, Y. J. Yoon, J. W. Kim, J. Lee, D. Huh, H. Lee, S. K. Kwak, J. Y. Kim, D. S. Kim, *Joule* **2019**, *3*, 2179.
[25] S. Liu, D. Zhang, Y. Sheng, W. Zhang, Z. Qin, M. Qin, S. Li, Y. Wang, C. Gao, Q. Wang, Y. Ming, C. Liu, K. Yang, Q. Huang, J. Qi, Q. Gao, K. Chen, Y. Hu, Y. Rong, X. Lu, A. Mei, H. Han, *Fundam. Res.* **2022**, *2*, 276.
[26] P. Wang, X. Zhang, Y. Zhou, Q. Jiang, Q. Ye, Z. Chu, X. Li, X. Yang, Z. Yin, J. You, *Nat. Commun.* **2018**, *9*, 2225.
[27] D. Liu, S. Wang, R. Xia, Y. Xu, L. Gu, R. Li, X. Fang, H. Hu, N. Yuan, J. Ding, *ACS Appl. Mater. Interfaces* **2021**, *13*, 11783.
[28] L. Zuo, H. Guo, D. W. deQuilettes, S. Jariwala, N. De Marco, S. Dong, R. DeBlock, D. S. Ginger, B. Dunn, M. Wang, Y. Yang, *Sci. Adv.* **2017**, *3*, e1700106.
[29] C. Chen, X. Wang, Z. Li, X. Du, Z. Shao, X. Sun, D. Liu, C. Gao, L. Hao, Q. Zhao, B. Zhang, G. Cui, S. Pang, *Angew. Chem., Int. Ed.* **2022**, *61*, e202113932.
[30] Y. Zhao, J. Wei, H. Li, Y. Yan, W. Zhou, D. Yu, Q. Zhao, *Nat. Commun.* **2016**, *7*, 10228.
[31] X. Duan, X. Li, L. Tan, Z. Huang, J. Yang, G. Liu, Z. Lin, Y. Chen, *Adv. Mater.* **2020**, *32*, 2000617.
[32] T. Li, S. Wang, J. Yang, X. Pu, B. Gao, Z. He, Q. Cao, J. Han, X. Li, *Nano Energy* **2021**, *82*, 105742.
[33] T. H. Han, J. W. Lee, C. Choi, S. Tan, C. Lee, Y. Zhao, Z. Dai, N. De Marco, S. J. Lee, S. H. Bae, Y. Yuan, H. M. Lee, Y. Huang, Y. Yang, *Nat. Commun.* **2019**, *10*, 520.
[34] Z. Li, M. Wu, L. Yang, K. Guo, Y. Duan, Y. Li, K. He, Y. Xing, Z. Zhang, H. Zhou, D. Xu, J. Wang, H. Zou, D. Li, Z. Liu, *Adv. Funct. Mater.* **2023**, https://onlinelibrary.wiley.com/doi/10.1002/adfm.202212606.
[35] Z. Gu, Z. Huang, C. Li, M. Li, Y. Song, *Sci. Adv.* **2018**, *4*, eaat2390.
[36] M. J. McCann, K. R. Catchpole, K. J. Weber, A. W. Blakers, *Sol. Energy Mater. Sol. Cells* **2001**, *68*, 135.
[37] C. Liu, S. Liu, Y. Wang, Y. Chu, K. Yang, X. Wang, C. Gao, Q. Wang, J. Du, S. Li, Y. Hu, Y. Rong, L. Guo, A. Mei, H. Han, *Adv. Funct. Mater.* **2021**, *31*, 2010603.
[38] X. Luo, Z. Shen, Y. Shen, Z. Su, X. Gao, Y. Wang, Q. Han, L. Han, *Adv. Mater.* **2022**, *34*, 2202100.
[39] T. Walter, R. Herberholz, C. Müller, H. W. Schock, *J. Appl. Phys.* **1996**, *80*, 4411.
[40] Z. Ni, C. Bao, Y. Liu, Q. Jiang, W.-Q. Wu, S. Chen, X. Dai, B. Chen, B. Hartweg, Z. Yu, Z. Holman, J. Huang, *Science* **2020**, *367*, 1352.
[41] Y. Shao, Z. Xiao, C. Bi, Y. Yuan, J. Huang, *Nat. Commun.* **2014**, *5*, 5784.
[42] N. Ahn, D. Y. Son, I. H. Jang, S. M. Kang, M. Choi, N. G. Park, *J. Am. Chem. Soc.* **2015**, *137*, 8696.
[43] D. H. Kang, C. Ma, N. G. Park, *ACS Appl. Mater. Interfaces* **2022**, *14*, 8984.
[44] D. Bi, C. Yi, J. Luo, J.-D. Décoppet, F. Zhang, S. M. Zakeeruddin, X. Li, A. Hagfeldt, M. Grätzel, *Nat. Energy* **2016**, *1*, 16142.
[45] S. Xiong, Z. Hou, S. Zou, X. Lu, J. Yang, T. Hao, Z. Zhou, J. Xu, Y. Zeng, W. Xiao, W. Dong, D. Li, X. Wang, Z. Hu, L. Sun, Y. Wu, X. Liu, L. Ding, Z. Sun, M. Fahlman, Q. Bao, *Joule* **2021**, *5*, 467.
[46] W.-J. Yin, T. Shi, Y. Yan, *Appl. Phys. Lett.* **2014**, *104*, 063903.
[47] X. H. Luo, X. S. Lin, F. Gao, Y. Zhao, X. D. Li, L. Q. Zhan, Z. X. Qiu, J. Wang, C. Chen, L. Meng, X. F. Gao, Y. Zhang, Z. J. Huang, R. D. Fan, H. F. Liu, Y. R. Chen, X. X. Ren, J. H. Tang, C. H. Chen, D. Yang, Y. G. Tu, X. Liu, D. X. Liu, Q. Zhao, J. B. You, J. F. Fang, Y. Z. Wu, H. W. Han, X. D. Zhang, D. W. Zhao, et al., *Sci. China Chem.* **2022**, *65*, 2369.

[48] Y. Cai, J. Cui, M. Chen, M. Zhang, Y. Han, F. Qian, H. Zhao, S. Yang, Z. Yang, H. Bian, T. Wang, K. Guo, M. Cai, S. Dai, Z. Liu, S. Liu, *Adv. Funct. Mater.* **2020**, *31*, 2005776.
[49] Y. Gao, *Mater. Sci. Eng., R* **2010**, *68*, 39.
[50] Q. Wang, Y. Shao, H. Xie, L. Lyu, X. Liu, Y. Gao, J. Huang, *Appl. Phys. Lett.* **2014**, *105*, 163508.
[51] H. Chen, K. Li, H. Liu, Y. Gao, Y. Yuan, B. Yang, C. Zhou, *Org. Electron.* **2018**, *61*, 119.
[52] F. T. Pei, N. X. Li, Y. H. Chen, X. X. Niu, Y. Zhang, Z. Y. Guo, Z. J. Huang, H. C. Zai, G. L. Liu, Y. M. Zhang, Y. Bai, X. Zhang, C. Zhu, Q. Chen, Y. Li, H. P. Zhou, *ACS Energy Lett.* **2021**, *6*, 3029.
[53] T. Shi, S. Lin, M. Fang, D. Kong, Y. Yuan, Y. Gao, B. Yang, H. Han, C. Zhou, *Appl. Phys. Lett.* **2020**, *117*, 163501.
[54] X. Zheng, B. Chen, J. Dai, Y. Fang, Y. Bai, Y. Lin, H. Wei, X. C. Zeng, J. Huang, *Nat. Energy* **2017**, *2*, 17102.
[55] W. Tress, M. Yavari, K. Domanski, P. Yadav, B. Niesen, J. P. Correa Baena, A. Hagfeldt, M. Graetzel, *Energy Environ. Sci.* **2018**, *11*, 151.
[56] Y. Yuan, Q. Wang, Y. Shao, H. Lu, T. Li, A. Gruverman, J. Huang, *Adv. Energy Mater.* **2016**, *6*, 1501803.
[57] H. Chen, H. Wang, Y. Xue, Q. Ge, Y. Du, J. Yin, B. Yang, S. Yang, X. Liu, M. Cai, S. Dai, *Chem. Eng. J.* **2022**, *450*, 138028.
[58] H. Kim, S. U. Lee, D. Y. Lee, M. J. Paik, H. Na, J. Lee, S. I. Seok, *Adv. Energy Mater.* **2019**, *9*, 1902740.
[59] J. Jeong, M. Kim, J. Seo, H. Lu, P. Ahlawat, A. Mishra, Y. Yang, M. A. Hope, F. T. Eickemeyer, M. Kim, Y. J. Yoon, I. W. Choi, B. P. Darwich, S. J. Choi, Y. Jo, J. H. Lee, B. Walker, S. M. Zakeeruddin, L. Emsley, U. Rothlisberger, A. Hagfeldt, D. S. Kim, M. Gratzel, J. Y. Kim, *Nature* **2021**, *592*, 381.
[60] M. S. de Holanda, R. Szostak, P. E. Marchezi, L. G. T. A. Duarte, J. C. Germino, T. D. Z. Atvars, A. F. Nogueira, *Sol. RRL* **2019**, *3*, 1900199.
[61] S. Sidhik, Y. Wang, M. De Siena, R. Asadpour, A. J. Torma, T. Terlier, K. Ho, W. Li, A. B. Puthirath, X. Shuai, A. Agrawal, B. Traore, M. Jones, R. Giridharagopal, P. M. Ajayan, J. Strzalka, D. S. Ginger, C. Katan, M. A. Alam, J. Even, M. G. Kanatzidis, A. D. Mohite, *Science* **2022**, *377*, 1425.
[62] A. A. Sutanto, P. Caprioglio, N. Drigo, Y. J. Hofstetter, I. Garcia-Benito, V. I. E. Queloz, D. Neher, M. K. Nazeeruddin, M. Stolterfoht, Y. Vaynzof, G. Grancini, *Chem* **2021**, *7*, 1903.